Tissue Eng Regen Med (2022) 19(4):739–754
https://doi.org/10.1007/s13770-022-00447-3

Online ISSN 2212-5469

ORIGINAL ARTICLE

Development of a Novel Perfusion Rotating Wall Vessel Bioreactor with Ultrasound Stimulation for Mass-Production of Mineralized Tissue Constructs

Jae Min Cha[1,2] · Yu-Shik Hwang[3] · Dong-Ku Kang[4] · Jun Lee[5] · Elana S. Cooper[6] · Athanasios Mantalaris[6]

Received: 6 February 2022 / Revised: 6 February 2022 / Accepted: 20 February 2022 / Published online: 9 May 2022

Abstract

BACKGROUND: As stem cells are considered a promising cell source for tissue engineering, many culture strategies have been extensively studied to generate *in vitro* stem cell-based tissue constructs. However, most approaches using conventional tissue culture plates are limited by the lack of biological relevance in stem cell microenvironments required for neotissue formation. In this study, a novel perfusion rotating wall vessel (RWV) bioreactor was developed for mass-production of stem cell-based 3D tissue constructs.

METHODS: An automated RWV bioreactor was fabricated, which is capable of controlling continuous medium perfusion, highly efficient gas exchange with surrounding air, as well as low-intensity pulsed ultrasound (LIPUS) stimulation. Embryonic stem cells encapsulated in alginate/gelatin hydrogel were cultured in the osteogenic medium by using our bioreactor system. Cellular viability, growth kinetics, and osteogenesis/mineralization were thoroughly evaluated, and culture media were profiled at real time. The *in vivo* efficacy was examined by a rabbit cranial defect model.

RESULTS: Our bioreactor successfully maintained the optimal culture environments for stem cell proliferation, osteogenic differentiation, and mineralized tissue formation during the culture period. The mineralized tissue constructs produced by our bioreactor demonstrated higher void filling efficacy in the large bone defects compared to the group implanted with hydrogel beads only. In addition, the LIPUS modules mounted on our bioreactor successfully reached higher mineralization of the tissue constructs compared to the groups without LIPUS stimulation.

CONCLUSION: This study suggests an effective biomanufacturing strategy for mass-production of implantable mineralized tissue constructs from stem cells that could be applicable to future clinical practice.

Keywords Rotating wall vessel bioreactor · Perfusion · Stem cells · Low-intensity ultrasound · 3D mineralized tissue constructs

✉ Jae Min Cha
j.cha@inu.ac.kr

✉ Athanasios Mantalaris
sakis.mantalaris@gatech.edu

[1] Department of Mechatronics Engineering, College of Engineering, Incheon National University, 119 Academy-ro, Yeonsu-gu, Incheon 22012, Republic of Korea

[2] 3D Stem Cell Bioengineering Laboratory, Research Institute for Engineering and Technology, Incheon National University, Incheon 22012, Republic of Korea

[3] Department of Maxillofacial Biomedical Engineering and Institute of Oral Biology, School of Dentistry, Kyung Hee University, Seoul 02447, Republic of Korea

[4] Department of Chemistry, Research Institute of Basic Sciences, Incheon National University, Incheon 22012, Republic of Korea

[5] Wonkwang Bone Regeneration Research Institute, Wonkwang University, Iksan 570-749, Republic of Korea

[6] Department of Biomedical Engineering, Georgia Institute of Technology, Atlanta, GA 30332, USA

1 Introduction

Traditional stem cell culture methods using two-dimensional (2D) culture plates are unable to recapitulate the 3D microenvironments where stem cells innately reside [1–3]. In addition to the restricted surface area, general culture processes tend to be fragmented and labor-intensive, which could lead to difficulties in generating clinically relevant numbers of stem cells to support neotissue formation [1, 4]. Static culture conditions within these 2D environments often generate spatially heterogeneous gradients of physicochemical parameters in the culture environment due to a lack of mixing. Ultimately, this will limit the overall structural integration of cellular tissue constructs [5–7]. It was reported that the deposition of a mineralized matrix from stromal osteoblasts statically cultured in poly (DL-lactic-co-glycolic acid) foams only reached a depth of 240 μm and displayed a hypoxic necrotic center within the construct core [8]. Additionally, culturing chondrocytes on poly (glycolic acid) meshes under static conditions resulted in inhomogeneous glycosaminoglycan deposition restricted to the periphery of the construct [9]. To overcome these limitations, stirred-tank bioreactors have been used in a variety of studies to generate a convective flow that would allow for culturing of 3D tissue constructs with enhanced mass transport of oxygen, nutrients, and metabolites [10–16]. However, impellers used within these bioreactors for mixing can cause a disruptive effect on cells/tissues by turbulent flow generated from unpredictable shear forces [17–20]. Alternatively, a rotating wall vessel (RWV) bioreactor system presents a micro-gravity environment in culture that allows for efficient mixing and turbulence-free conditions where 3D tissue constructs can be stably grown over an extended culture period [21–25].

Our group previously reported a large scale production of mineralized tissue constructs based on 3D-osteogenesis of embryonic stem cells (ESCs), which was achieved by an integrated stem cell bioprocess using a RWV bioreactor [7, 23, 25]. The fed-batch culture system used in these previous studies, however, did not optimize cellular responses over long-term culture [26]. When whole culture medium was exchanged for regular-feeding or to induce differentiation, stem cells unavoidably experienced an abrupt change in culture environment (Fig. 1A, B). With proliferating cells, nutrients and oxygen would be exhausted faster, thus contributing to cellular stress. Furthermore, increased accumulation of metabolic wastes would create toxicity to the cells within culture [6, 27]. Therefore, continuous medium perfusion is now considered an essential feature for a bioreactor system. Continuous feeding more efficiently transfers nutrient/oxygen supply and medium supplementations for the large-scale and long-term culture of stem cell-derived tissue constructs (Fig. 1C, D) [28]. Several studies about engineering bone tissues from pluripotent stem cells using decellularized bone scaffolds and a perfusion bioreactor reported that mechanically-functional bone grafts were successfully grown *in vitro*, and after implantation, the engineered bone

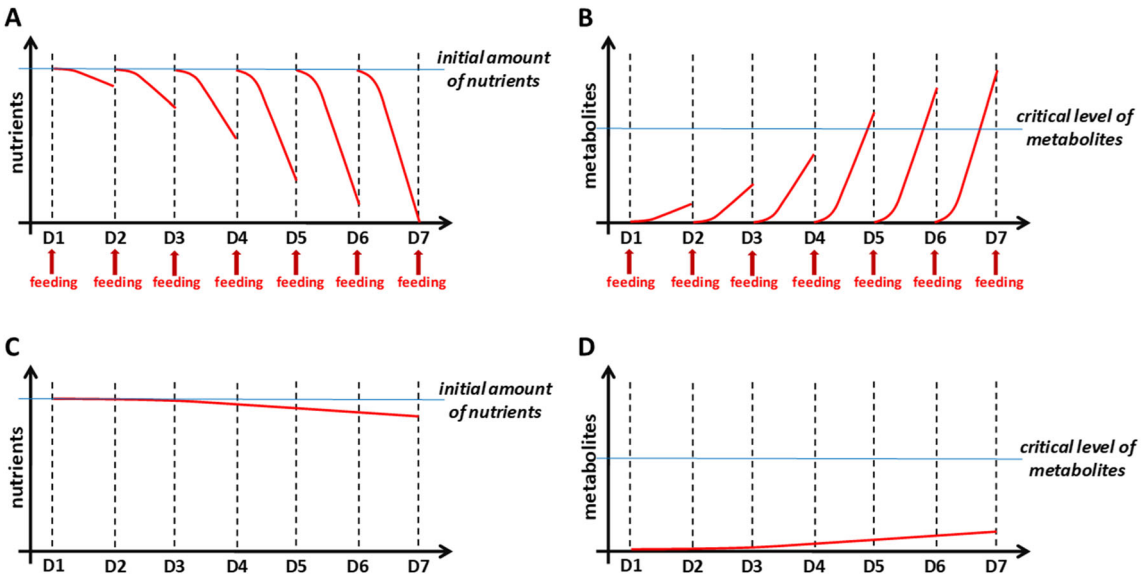

Fig. 1 Need for perfusion culture system. **A**, **B** Fed-batch bioreactors are problematic in the maintenance of a desirable culture environment due to the exhaustion of nutrients (**A**) and accumulation of toxic cellular metabolites (**B**). As cells grow over the culture time, cells in a fed-batch bioreactor can be more stressed by the abrupt exposure to a different culture environment caused by the exchange of medium. **C**, **D** Perfusion culture systems continuously supply the nutrients (**C**), prevent metabolic waste accumulation (**D**), and eliminate the potential stress caused by medium-exchange, facilitating the maintenance of a desirable environment

grafts were stably sustained *in vivo* with showing clues of continual bone tissue formation [29, 30]. However, the laborious and complex culture procedures required skilful operator handling to avoid experimental interferences. Although these approaches are reported to be successful, a more-streamlined, less-error-prone approach is needed within the field of bioprocessing for scalable production of engineered tissues.

The application of mechanical stimulation is a crucial factor for modulating cell physiology based on the wide-ranging effects of intracellular signalling on tissue homeostasis [31]. Bone cells are highly mechano-responsive and have the keen ability to alter their shape and thereby phenotype after being exposed to mechanical loading [32]. Previous studies have reported that the low-intensity pulsed ultrasound (LIPUS) stimulation that could avoid thermal effects on cells resulted in accelerated osteogenesis, showing some similar effects with mechanical loading on bone formation *in vivo* [33]. While the mechanisms of LIPUS-stimulated osteogenesis are not fully understood yet, it was suggested that shear stresses caused by acoustic radiation force and propagation of surface waves may trigger a biological response of osteoblasts with activating mechano-receptors on the cell membranes, i.e. activation of calcium ion channels [34]. As an immediate and non-invasive mechanical stimulation upon cell membrane, the LIPUS has been often applied to trigger or stimulate osteogenic cell proliferation and differentiation *in vitro*, and widely used in various orthopaedic clinical cases, as approved by the USA Food and Drug Administration, to promote bone fracture healing [35–38]. With the unprecedented growth of research and clinical needs for bone tissue engineering in recent years, the LIPUS could be a promising approach that can be used to manufacture implantable bone tissues from stem cells as enhancing osteogenesis and mineralization of the tissue constructs.

Herein, we present a novel perfusion RWV bioreactor system (named 'BSEL' for Biomedical Systems Engineering Laboratory) that can support stem cell growth, osteogenic differentiation, and 3D bone tissue growth in an automated and scalable manner. By using our BSEL bioreactor, ESCs were cultured over a long-term period following an established osteogenic differentiation protocol [39, 40], and the scalable production of mineralized 3D tissue constructs was successfully achieved. Culturing parameter profiles, cellular growth kinetics, osteogenic differentiation, mineralization, and mechanical strength of the resulting tissue constructs were compared with those from a fed-batch RWV bioreactor and static culture condition. A pilot animal study was conducted to demonstrate the feasibility of the mineralized tissue constructs produced by our bioreactor to address critical size cranial bone defects in rabbits. The application of mechanical loading via customized LIPUS stimulation modules to the BSEL bioreactor further enhanced osteogenic differentiation and mineralization of ESC-tissue constructs. We established a scalable perfusion-based biomanufacturing platform (BSEL bioreactor) with the LIPUS stimulation of ESC-encapsulated alginate microbeads that demonstrates potential for therapeutic bone healing and repair.

2 Materials and methods

2.1 Cell culture

Murine ESCs (E14Tg2α, ATCC, Manassas, VA, USA) were routinely cultured following the protocols described in our previous study [39]. Briefly, undifferentiated ESCs (< passage 20) were passaged every 2 or 3 days and fed every day with the fresh maintenance medium based on high glucose Dulbecco's Modified Eagle Medium (DMEM) without sodium pyruvate (Invitrogen, Paisley, UK) containing 10% (v/v) of fetal bovine serum (FBS) batch-tested (Invitrogen), 1% (v/v) of penicillin and streptomycin (Invitrogen), 2 mM of L-glutamine (Invitrogen), 0.1 μM of 2-mercaptoethanol (Sigma-Aldrich, Poole, UK) and 1000 units/ml of Leukemia Inhibitory Factor (LIF) (Chemicon, Hampshire, UK). HepG2 cells (HB-8605, ATCC) were cultured with DMEM containing 10% (v/v) FBS and 1% (v/v) of penicillin and streptomycin. The culturing medium was not changed for the following 4 days and then collected to the 0.22-μm filter-unit (VWR International, Poole, UK) for filter-sterilization followed by supplementing 0.1 μM of 2-mercaptoethanol and 2 mM of L-glutamine. In order to enhance osteogenic differentiation through the selective mesodermal development from ESCs, HepG2-conditioned medium (HepG2-CM) was used in this study as described in the previous studies [7, 39, 40].

2.2 Design and fabrication of perfusion RWV bioreactor (BSEL)

All parts and dimensions of the BSEL bioreactor were designed using Solid Works. The base plate materials and cases for motor units were Derlin/Acetyl plastics (Metal & Plastic Ltd., Hertfordshire, UK), electric components were fully sealed with silicone rubber to avoid corrosion. Universal 500 ml glass bottles (Fisher Scientific, Leicestershire, UK) were used for the fresh/waste medium bottles, and medium perfusion tubes were made of silicon (Fisher Scientific). The culture vessel was covered with a thin gas-permeable membrane made of silicon (outside) and polytetrafluoroethylene (PTFE, inside) (Specialty Silicon Products Inc., NY, USA). The external oxygenator is composed of a spiral roll of thin gas-permeable silicon

tubing with a wall thickness of 0.5 mm. The length of the tubing roll was designed to saturate the culture medium with oxygen while the medium passes through the oxygenator (3.4 m). All the parts of this bioreactor can be disassembled and sterilized by autoclave apart from the motors and pumps.

2.3 3D-culture conditions to grow mineralized tissue constructs

Undifferentiated ESCs were encapsulated in alginate hydrogels (beads) as described in our previous study [25]. Encapsulated cells were subsequently transferred to three different 3D-culture conditions: a static condition (Static, 150 mm petri-dish), fed-batch RWV bioreactor (55-ml High Aspect Ratio Vessel (HARV), Cellon, Bereldange, Luxembourg), and BSEL bioreactor (about 500 beads in each condition). After the cultures started, the HARV and Static groups were fed with 55 ml of HepG2-CM every day for the first three days. The BSEL bioreactor was setup to feed cells by continuous HepG2-CM perfusion at a rate of 0.7 µl/s (approximately 60 ml/day) for 3 days. Osteogenic differentiation was triggered on day 4 following the osteogenesis protocol in the previous studies [39, 40]. During this period, 55 ml of osteogenic media in the HARV and Static groups were exchanged every 2 days. The BSEL bioreactor started medium perfusion at a rate of 0.7 µl/s when the media in the HARV and Static groups were exchanged. The medium perfusion was suspended after 24 h until the next feeding time of the HARV and Static groups, thus enabling a similar amount of osteogenic medium supply in total.

2.4 Live/dead assay of encapsulated ESCs

Viability of encapsulated ESCs was evaluated using LIVE/DEAD Viability/Cytotoxicity Kit (Invitrogen). Collected tissue constructs were washed with PBS, and then cell viability was tested following the manufacturer's instruction of the kit.

2.5 Media profiling analysis for different 3D-culture conditions

Culture media from all groups were collected during the culture period and analyzed by measuring glucose, lactate, ammonia, glutamine, and pH using BioProfile Analyser 400 (Nova Biomedical, MA, USA). The fresh culture medium was measured as a control and indicated in each plot by a dotted line. Oxygen was measured using Dissolved Oxygen Meter (Extech Instruments Co., MA, USA). A tailor-made socket was used to avoid the collected medium being exposed to air while oxygen tension was measured. As a control, the initial oxygen tension in culture medium was measured and indicated in the plot by a dotted line. All cultures for medium-profiling were carried out separately from other assays.

2.6 DNA quantification for evaluation of expansion of encapsulated ESCs

After collecting ten tissue constructs from each group (n = 3), the samples were dissolved in the depolymerization buffer consisting of 50 mM tri-sodium citrate dihydrate (Fluka, Poole, UK), 77 mM sodium chloride (BDH Laboratories Supplies, Poole, UK) and 10 mM HEPES (Sigma-Aldrich). Isolated cells were digested in 50 µg/ml proteinase-K (Sigma-Aldrich) solution based on 100 mM dibasic potassium phosphate, pH 8.0 (K_2HPO_4; Sigma-Aldrich) overnight at 37 °C. Proteinase-K was inactivated by heating at 90 °C for 10 min. Total DNA contents were measured using Quant-iT PicoGreen dsDNA Reagent and Kits (Invitrogen), following the manufacturer's instruction. The amount of total DNA produced from routinely cultured ESCs was quantified in order to calibrate the number of cells per sample.

2.7 Gene expression analysis

After dissolving tissue constructs, total RNAs from the samples were extracted by using RNeasy kit (Qiagen, West Sussex, UK), according to the manufacturer's instructions. For quantitative polymerase chain reaction (qPCR), 80 ng of RNA sample was added in each reaction based on the manufacturer's instruction of SensiMix™ One-Step Kit (Quantace, London, UK). The relative quantifications were conducted based on the $2^{-\Delta\Delta CT}$ method [41]. For reverse transcription (RT) PCR, cDNA was synthesized following the manufacturer's instruction (Promega, Southampton, UK). 100 ng of cDNA samples were amplified with the PCR conditions previously set and analyzed on a 1.5% (w/v) agarose gel by ethidium bromide staining in ultra-violet light. The information of primers can be found in Table 1.

2.8 Alizarin Red S (ARS) assay for mineralization quantification

Mineralization of tissue constructs was quantified based on Alizarin Red S assay [42]. All detailed procedures can be found in our previous study [25].

2.9 Attenuated total reflections Fourier transform infrared (ATR-FTIR) analysis for hydroxyapatite composition

ATR-FTIR imaging analysis was conducted using a continuous scan FTIR spectrometer (Varian 7000 FT-IR, Varian Inc. CA, USA) in conjunction to a large sample

Table 1 Primer information

Genes	Sequences
Collagen I	(fwd) CGTGGCGACCAAGGTCCAGT
	(rvs) AGGGAGACCCAGAATACCGGGAG
Osterix	(fwd) TTGAGGAAGAAGCTCACTATGGCTCCAG
	(rvs) GCTGAAAGGTCAGCGTATGGCT
Runx2	(fwd) TCGTCAGCATCCTATCAGTTCCCA
	(rvs) CCATCAGCGTCAACACCATCATTCTGGTTAG
Osteonectin	(fwd) AGCACCCCATTGACGGGTA
	(rvs) GGTCACAGGTCTCGAAAAAGC
Osteocalcin	(fwd) GGACTGTGACGAGTTGGCTG
	(rvs) CCGTAGAAGCGCCGATAGG
Oct4	(fwd) GGC TTC AGA CTT CGC CTCC
	(rvs) AAC CTG AGG TCC ACA GTA TGC
Nanog	(fwd) CCT GAT TCT TCT ACC AGT CCCA
	(rvs) GGC CTG AGA GAA CAC AGT CC
GAPDH	(fwd) CATCACCATCTTCCAGGAGC
	(rvs) ATGCCAGTGAGCTTCCCGTC

compartment extension (Varian LS) and a 64 × 64 focal plane array (FPA) detector. Further details about the ATR-FTIR imaging setup can be found elsewhere [43]. Mineralized tissue constructs collected on day 29 were cut in half using a razor blade and placed onto the measuring surface of the ATR crystal (oil analyser, Specac Ltd., Kent, UK). Excess water was removed and the sample was enclosed to prevent further evaporation, thus ensuring that the tissue construct remained hydrated during the measurement. Spectra were acquired with 8 cm^{-1} spectral resolution with 32 co-adding scans. Five tissue constructs were measured from each group. Spectral data was analyzed using the Isys software (Spectral Dimension, Malvern, Aus). Factor analysis was applied to the spectral region of 1200–965 cm^{-1} in a similar manner as described in other work [44]. All results were analyzed simultaneously by concatenating all images together before applying factor analysis. The images showing the distribution of the hydroxyapatite in the tissue constructs were extracted using factor analysis. A binary image was generated with a threshold of 10% to outline the pixels that are considered to have detected hydroxyapatite. The relative amount of hydroxyapatite in each tissue construct was compared by calculating the percentage area that was registered with the presence of hydroxyapatite.

2.10 Mechanical strength testing of mineralized tissue constructs

A micro-deformation apparatus developed in previous publications [45, 46] was used to measure the force–displacement characteristics of the mineralized tissue constructs collected on day 29. The apparatus permits continuous and simultaneous measurements on the responsive force (measured with a cantilever transducer of 10 μN resolution) and the applied displacement (monitored by the computer with a resolution of 0.1 μm). The samples were subjected to a maximum deformation of up to 10%, and continuously monitored by a high-resolution video camera during manipulation and deformation to ensure that the bead structure was not damaged. Deformation measurements were carried out immediately after sample collection to minimize the effects on the tissue construct compliance due to swelling. At least thirteen force–displacement measurements were taken for each group, and all the experiments were conducted under ambient conditions (T = 20 ± 2 °C). Young's modulus for each group was calculated based on the measurements, and the mechanical strength (as stiffness) was compared.

2.11 *In vivo* implantation of mineralized tissue constructs

Adult New Zealand white rabbits approximately 3 kg in weight were used in this study (n = 4). All surgical procedures were performed in aseptic conditions according to the guidelines of the Animal Research Committee of Wonkwang University, Iksan, Korea. Before surgery, intramuscular injection of 2.0 mg/kg (body weight) of ketamine (Yuhan, Seoul, Korea) was administered, followed by the surgical procedures. The cranial area was shaved and local anesthesia administered using 1.8 ml of 2% (v/v) lidocane with 1:100,000 epinephrine. To avoid infection, a povidone iodine solution and drape were introduced within the surgical area. The scalp was incised and the cranium was widely exposed, creating four round-

shaped and standardized cranial defects (diameter: 8 mm, depth: 2–3 mm) (Supplementary Fig. S1A and B). All surgical procedures undertaken avoided the creation of defects in the dura or midsagittal sinus. Mineralized tissue constructs produced by the BSEL bioreactor were inserted into the defects (about ten tissue constructs per defect). Alginate beads without cells were introduced as a negative control. Fibrin glue was used to fix the grafts (Supplementary Fig. S1C and D). Periosteal approximation was undertaken with 4–0 nylon (Ethicon, Norderstedt, Germany) followed by dermal suture using 3–0 silk (Yuhan, Seoul, Korea). During the first 3 days, intramuscular antibiotic treatment [3 mg/kg (body weight) of Cefazedone, Sam Shin Chemical, Ansan, Korea] was applied to prevent infection. The rabbits were sacrificed using Urethane (Sigma-Aldrich) at 8 weeks.

2.12 Micro-focus X-ray computed tomography (micro-CT)

The images of the mineralized portions within the defects were obtained at 8 weeks by micro-CT scanning (Harmony 130G-P3-5, DRGEM Co., Seoul, Korea), set as 5 μm of focal spot size, 10.5 mm of field of view, reconstruction image size 2048 × 2048 pixels, 16 bit of depth of reconstruction image, and 130 kV of tube voltage. 3D-structures of the defects at 8 weeks were reconstructed using Cone-beam volumetric reconstruction algorithm.

2.13 Histological analysis of large bone defects

The cranial vaults were removed from rabbits at 8 weeks (Supplementary Fig. S1E). The conventional paraffin embedding and slide-sectioning procedures were then followed. Histological examinations were performed by haematoxylin and eosin (H&E) staining. Immunohistochemistry was performed with the sections of the samples at 8 weeks using anti-osteocalcin (Santa Cruz Biotech, Dallas, TX, USA).

2.14 LIPUS stimulation mounted on the BSEL bioreactor

The ultrasound system was custom-designed and supplied by Sigmax (Tokyo, Japan). The controller was also custom-designed to enable the ultrasound stimulation for the medical criteria as described in Table 2 and Supplementary Figure S2. Each ultrasound probe has an area of 0.53 cm^2 and the total ultrasound treatment area (four probes) is 2.12 cm^2 which covers around one-sixth of the vessel cross-section area. Ultrasound probes were placed into the culture chamber to ensure the direct contact between probe's surface and culture medium. From the concept of ultrasound reflection and transmission, the rear of the culture chamber was placed with an acoustic absorbing material, HAM-A (Precision Acoustics Ltd, Dorset, UK) consisting of polyurethane double layer. The top surface had a matching acoustic impedance to water and the base layer was partially air-loaded to increase the transmission loss. The HAM-A material's acoustic impedance was higher than the acoustic impedance of water; therefore, no reflection occurred at the back of the culture chamber and the single overlap was avoided (IEC61161, 1992). The cables connected to the ultrasound probes were wired to the rotating bearing to avoid the twisting of the ultrasound cables while the bioreactor rotated. Ultrasonic beam profiles were measured by the methods approved by the International Electrotechnical Commission (IEC61102, IEC62127, and IEC61689). The overall setup of the system was monitored and recorded by the Soniq Software which enabled real-time plotting.

2.15 Statistical analysis

Samples for the quantitative analyses were measured in a duplicate or triplicate manner. Error bars on all graphs represented the standard deviation (SD) of the mean. Each comparable value from each group was statistically analyzed with student t-test or analysis of variance (ANOVA) for each proper case at a level of significance of $p < 0.05$ or $p < 0.001$ (single or double asterisks respectively).

3 Results

3.1 Key features of perfusion RWV bioreactor system (BSEL)

An integrated 3D-culture bioprocess using the BSEL bioreactor established in this study is described in Fig. 2A. Briefly, an automated hydrogel encapsulator enabled the production of approximately 500 stem cell-laden alginate beads within 3 min (each bead contained about 20,000 cells). The encapsulated stem cells were grown at a large scale as mineralized tissue constructs using the BSEL bioreactor system. The BSEL bioreactor facilitated the maintenance of a desirable 3D-culture environment with the features of continuous oxygenation, supply of nutrients, and removal of metabolic waste along with the highly efficient gas exchange with the surrounding air. This system consisted of two culture vessels with a volume of 58 ml each (Fig. 2B). The culture vessel rotation was controlled by a single servo motor unit, generating a free-fall state for tissue constructs cultured inside the rotating vessels. Culture medium was perfused by micro-peristaltic pumps capable of controlling the perfusion rates of

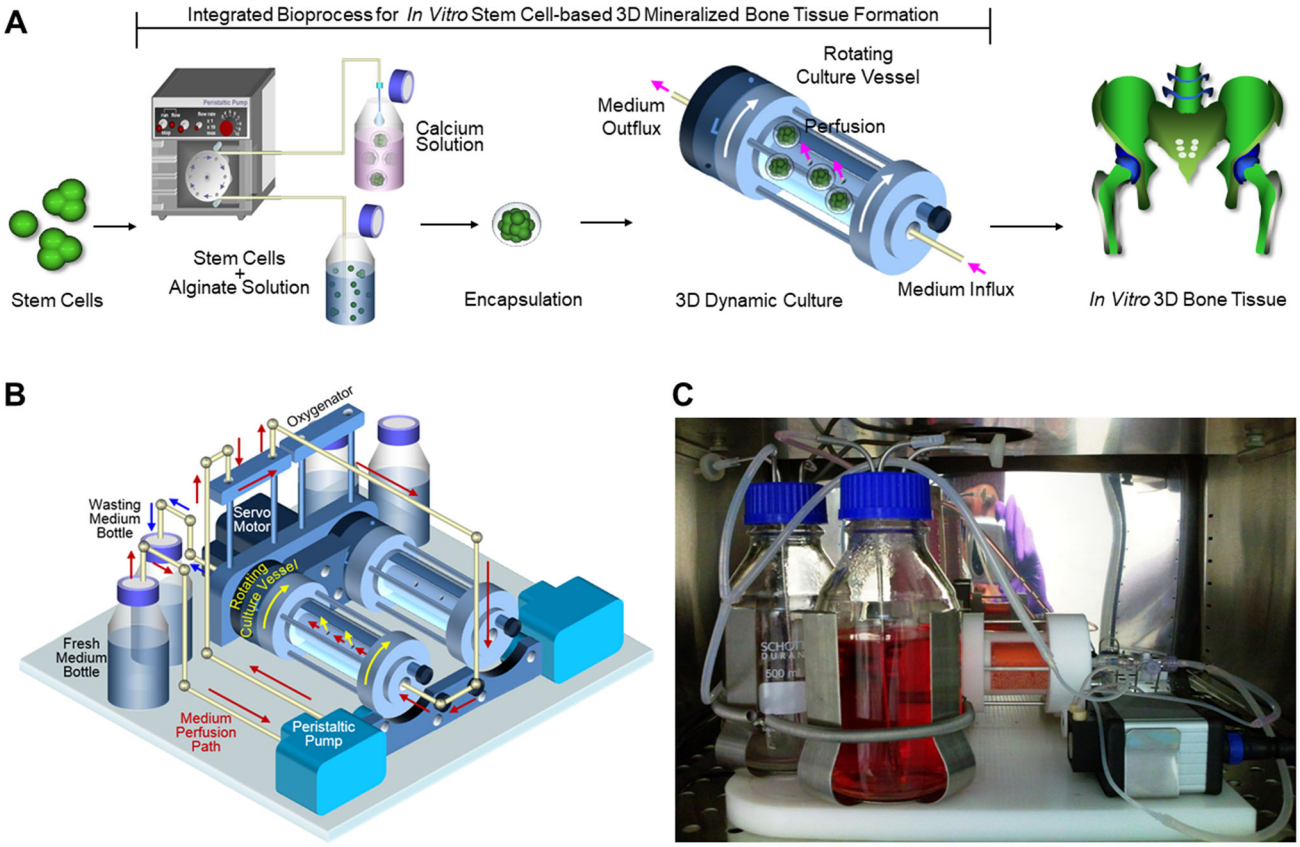

Fig. 2 Integrated bioprocess for 3D stem cell culture and a perfusion RWV bioreactor (BSEL) system. (**A**) Approximately five-hundreds of stem cell-laden alginate beads were produced within 3 min by an automated hydrogel encapsulator (each bead contained about 20,000 cells). Large scale production of stem cell-based 3D-tissue constructs was achieved by using a novel perfusion RWV bioreactor system. (**B**) Two sets of the perfusion RWV system were mounted on a single base unit, which rotated together by a servo motor (a perfusion path driven by a peristaltic pump is indicated by the red arrows: fresh medium bottle → oxygenator → culture vessel → wasting medium bottle). A gas-permeable membrane covered the culture vessel to have a direct gas-exchange with the surrounding air. **C** The bioreactor system running in a CO_2 incubator. Tissue constructs in the culture vessel were in a free-fall state while the culture vessel rotated

0.5–5 μl/s. The medium was channelled through a long thin-walled silicon tubing (oxygenator) prior to perfusion into the vessel. A gas-permeable membrane surrounds the culture vessel to provide efficient gas exchange with the surrounding air, which was double-layered with silicon (outside) and PTFE (inside) to reduce fouling effects from biomolecules. Gaseous tensions inside the culture vessel were quickly equilibrated with air in a CO_2 incubator through both the exterior oxygenator and gas-permeable membrane. The whole bioreactor system was mounted in a CO_2 incubator (Fig. 2C), and all the operations are controlled by a computer system setup outside the incubator.

3.2 Growth kinetics of encapsulated ESCs in different 3D-culture conditions

Encapsulated ESCs and their colonies growing in the BSEL bioreactor were observed under a microscope over the culture period. Cells were initially suspended at a single cell level and homogeneously distributed throughout the hydrogel (Fig. 3A). They were spontaneously aggregated, subsequently forming cellular colonies over the culture period (Fig. 3B, C). The hydrogel beads containing ESCs became visually opaque while fully packed with large cellular colonies on day 21 (Fig. 3D). Growth kinetics of encapsulated ESCs in different culture conditions were presented by measuring DNA quantity increment (Fig. 3E). Dynamic culture conditions (HARV and BSEL) showed faster growth rates than the Static group during the whole culture period. In particular, the BSEL group showed a significantly faster cellular expansion rate in the early stage of osteogenesis from day 5 to 9 ($p < 0.05$). However, the growth of encapsulated ESCs reached a stationary rate primarily due to the spatial restrictions in a hydrogel bead while the density of cells approached about 3.5×10^5 cells/bead. In situ cellular viability was assessed on day 21 showing the appearance of highly viable cell colonies growing in the hydrogel (Fig. 3F; green fluorescence in the representative photo).

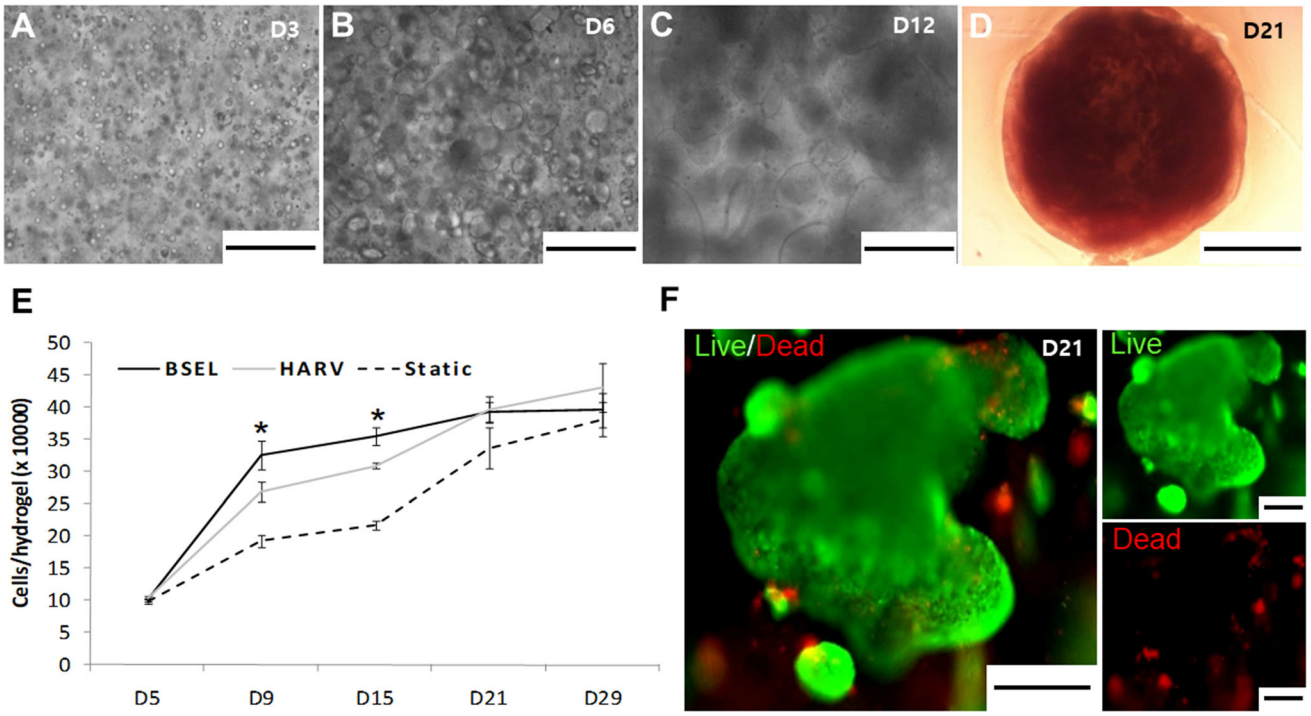

Fig. 3 Growth kinetics of encapsulated ESCs. **A**–**D** Microscopic observation of the ESC-colonies growing over the culture period. Scale bars are 500 μm on D3 (**A**), D6 (**B**), and D12 (**C**). The beads became visually opaque with fully packed ESC-colonies on D21 (**D**). The scale bar indicates 1000 μm. **E** Cellular growth kinetics of all 3D-culture conditions were examined by a DNA quantification method during the culture period. **F** Cell viability in the tissue constructs was examined on day 21 using a Live/Dead assay kit (live, green fluorescence; dead, red fluorescence). Scale bars are 200 μm

3.3 Profiling of culturing parameters in different 3D-culture conditions

Culture media were collected from different culture conditions and analyzed with a bioprofiler during the osteogenesis period (Fig. 4). A dotted line on each graph indicates the initial level of corresponding substance in the fresh medium. The BSEL group steadily maintained the pH levels at between 7.2 and 7.5 until the end of culture period, while the pH levels in the HARV group were significantly lowered at between 6.7 and 7 ($p < 0.05$) (Fig. 4A). The initial concentration of glucose in the expansion medium (HepG2-CM) was 12 mM (Fig. 4B). During the first 3 days of expansion period, the BSEL group maintained a significantly higher glucose level due to the continuous medium perfusion ($p < 0.05$). Afterwards, the medium was changed to the osteogenic medium whose initial level of glucose was 5.6 mM. During the osteogenic differentiation period, glucose was almost fully consumed in all groups. Corresponding to the glucose profiles, the HARV group showed a significantly higher level of lactate on day 3 ($p < 0.05$) (Fig. 4C). However, during the osteogenesis period, variation in the lactate levels was negligible in all groups, most likely related to lacking glucose in the osteogenic medium. Meanwhile, the glutamine levels in the BSEL group were maintained at significantly higher levels during the osteogenesis period ($p < 0.05$) (Fig. 4D). On the other hand, significantly higher levels of ammonia (NH_4^+) were accumulated in the HARV group during the osteogenesis period ($p < 0.05$), exceeding 3.5 mM (Fig. 4E). In addition, the oxygen levels in culture medium were also measured during the culture period (Fig. 4F). The oxygen levels in air (8.7 mg/l, approx. 20%) and the fresh osteogenic medium (5.6 mg/l) were also measured as the controls of comparison and indicated by dotted lines in the graph. The oxygen level in the HARV group tended to gradually decrease until the end of culture up to about 2.7 mg/l (4–5% in air), while the BSEL group maintained the oxygen levels close to the initial level.

3.4 Development of mineralized tissue constructs

In order to evaluate the extent of osteogenesis in the different 3D-culture conditions, the expression of several genes related to osteogenic differentiation such as type I collagen (Col1), Runx2 (RUNX2), and Osterix (Osx) were relatively quantified on day 29 (Fig. 5A–C). Gene expression levels of the BSEL and HARV groups were presented by normalization with those of the Static group.

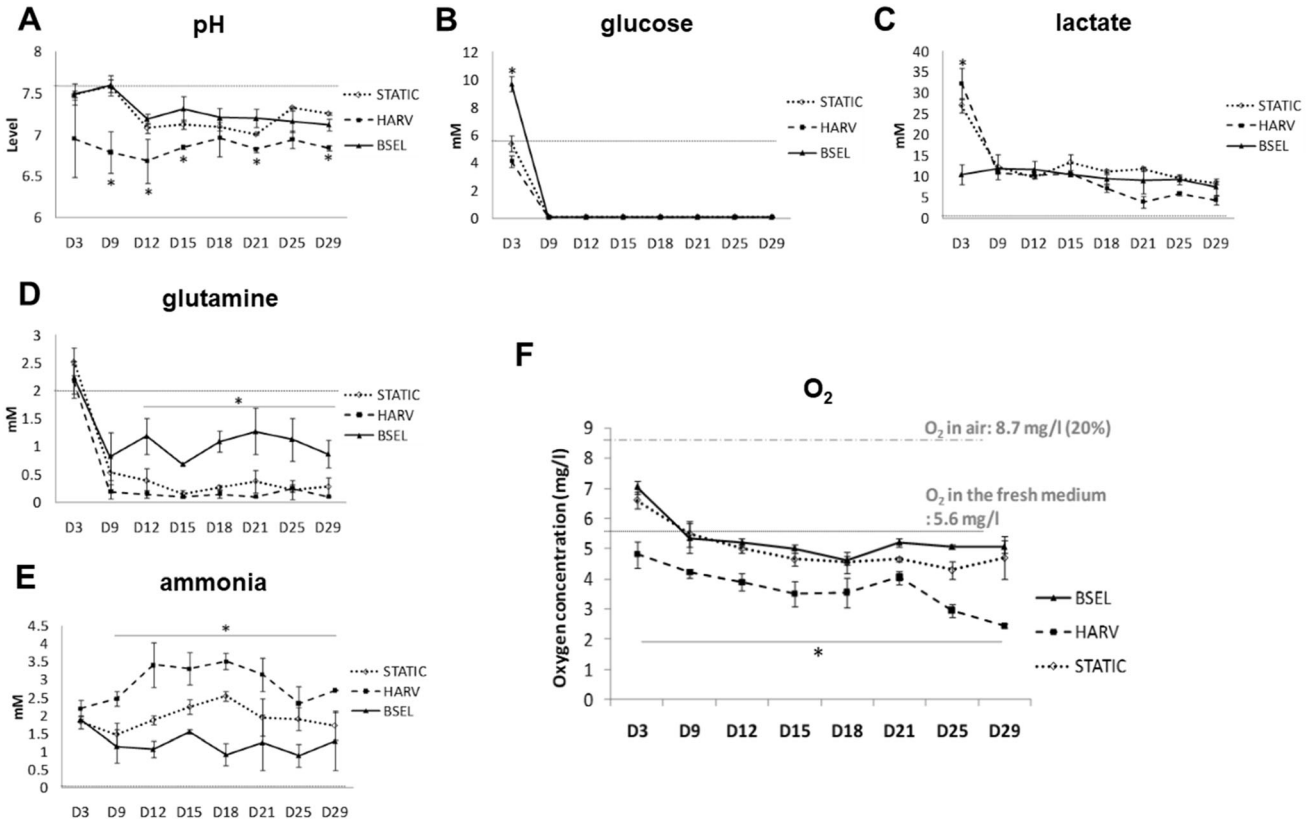

Fig. 4 Profiling of culturing factors in the 3D-culture conditions. Culture media from all groups were collected during the culture period and the bioprofile information was analyzed by measuring **A** pH, **B** glucose, **C** lactate, **D** glutamine, and **E** ammonia, and **F** oxygen. The fresh culture medium was measured as a control and indicated in each plot by a dotted line. All the statistics were done between the BSEL and HARV groups by a student *t* test (n = 3). All error bars are standard deviation (SD). Asterisks indicate $p < 0.05$

Significant differences between the HARV and BSEL groups were not found in the Col1 and RUNX2 expressions, nevertheless showing significantly higher expressions than the Static group (a level of 1.0) (Fig. 5A, B). In the Osx expression, the BSEL group showed a significantly higher expression than the HARV group ($p < 0.001$) (Fig. 5C). The expressions of pluripotency gene markers, Oct4 and Nanog, were investigated to assess a residual population of pluripotent stem cells in the mineralized tissues developed in the BSEL bioreactor (Fig. 5D). The osteogenic gene markers, such as Osx and RUNX2, were simultaneously validated. Encapsulated ESCs cultured with leukemia inhibitory factor (LIF) for 13 days in the BSEL bioreactor were used as a control group for the comparison. The control group (a) expressed both the pluripotency gene markers without the expressions of osteogenic gene markers. On the contrary, in the mineralized tissue constructs developed by the BSEL bioreactor (b), the expression of pluripotency gene markers were hardly found. Mineralization in all groups was quantified by the ARS quantification analysis (Fig. 5E). The BSEL and HARV groups showed significantly higher accumulation of the calcified matrix deposition than the Static group on day 21 ($p < 0.05$). After dexamethasone supplementation on day 21, the largely accelerated mineralization was shown in both of the dynamic culture conditions, the HARV and BSEL groups. In particular, mineralization in the BSEL group was shown to be the highest on day 29 among all groups, 8-times higher compared to the Static group ($p < 0.001$).

Spatial hydroxyapatite composition in the mineralized tissue constructs was analyzed and quantified by ATR-FTIR imaging analysis. The infrared images in which an entire bead was displayed were captured in the spectral region of 1200–965 cm^{-1} (Fig. 6A). The color gradient from yellow to red represents the extent of approaching to the peak in the spectra (PO_4 at between 1026 and 1035 cm^{-1}). Photographs of the whitened mineralized tissue constructs collected from the BSEL group on day 29 were shown in Fig. 6B. Cumulative hydroxyapatite was compared by calculating percentage of the areas that were registered as the presence of hydroxyapatite (Fig. 6C). The hydrogels containing undifferentiated ESCs (control) were measured as a negative control. In the infrared image analysis, the BSEL group was shown to have the highest composition of hydroxyapatite among all groups. The

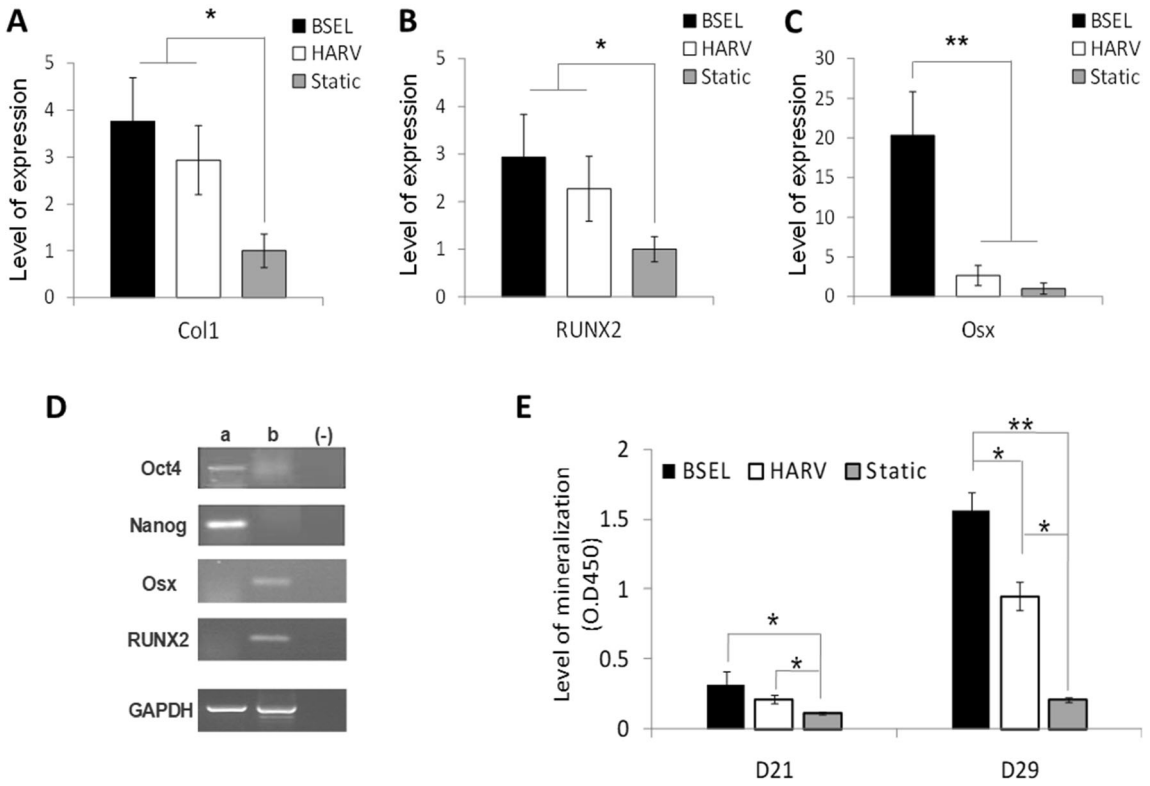

Fig. 5 Analyses of osteogenic differentiation and mineralization. Osteogenic constructs were collected at the end of culture period (D29) from all 3D-culture conditions. **A**–**C** Comparisons of osteogenic gene expressions: **A** type I collagen (Col1), **B** Runx2 (RUNX2), and **C** Osterix (Osx). All quantitative comparisons were normalized by the correspondent gene expression level of the Static group based on the $2^{-\Delta\Delta CT}$ method. Statistical analysis was performed by one-way ANOVA (n = 5) at a level of significance of $p < 0.05$ or $p < 0.001$ (single and double asterisks, respectively). All error bars represent standard deviation (SD). **D** Verification of pluripotency marker gene expression of Oct4 and Nanog; **a** pluripotent samples 3D-cultured for 13 days in the BSEL bioreactor using the medium containing the leukemia inhibitory factor (LIF); **b** osteogenic samples cultured for 29 days in the BSEL bioreactor following the osteogenic differentiation protocol; (−) negative control (water blank). **E** Comparison of mineralization of the 3D-culture groups based on a quantitative Alizarin Red S (ARS) assay. Statistical analysis was performed by one-way ANOVA (n = 5) at a level of significance of $p < 0.05$ or $p < 0.001$ (single and double asterisks, respectively). All error bars represent standard deviation (SD)

occupancy of hydroxyapatite in the BSEL group was approximately five times higher than that of the HARV group ($p < 0.05$). The control group showed few red spots in the image indicating nearly 0% of hydroxyapatite composition. In order to examine how mineralization and hydroxyapatite composition contributed to the mechanical strength of the mineralized tissue constructs, mechanical compression testing was conducted (Fig. 6D). Based on the force–displacement plot fitted by linear regression, Young's moduli were calculated and compared among all groups (Table 3). The Young's modulus of an alginate hydrogel without cells (Alginate bead) was obtained as a standard of basic material. A control group (Control) was separately set using hydrogels encapsulating undifferentiated ESCs with a similar cell density (about 3.5–4 × 10^5 cells/bead). As a result, the BSEL group showed about 2.6-times and 6.2-times higher Young's modulus than the HARV and Static groups, respectively. Overall, mineralized tissue constructs developed in 3D-culture conditions, regardless of their type, had higher stiffness than Alginate bead and Control groups.

3.5 *In vivo* efficacy of the mineralized tissue constructs in the large bone defect animal model

Mineralized tissue constructs fabricated by the BSEL bioreactor were implanted in critical-sized cranial defects of adult New Zealand rabbits (Supplementary Fig. S1; data were presented in supplementary results as a pilot animal testing). The large bone defects were implanted with the mineralized tissue constructs and displayed relatively higher void filling efficacy in eight weeks compared to a negative control that showed mineralization only on the edge and dura mater areas (Supplementary Fig. S3A and B). In histology samples, the integrity of new bone tissues appeared to be higher in the defects implanted with the mineralized tissue constructs (Supplementary Fig. S3C(I) and D(I)). Immunohistochemistry data for

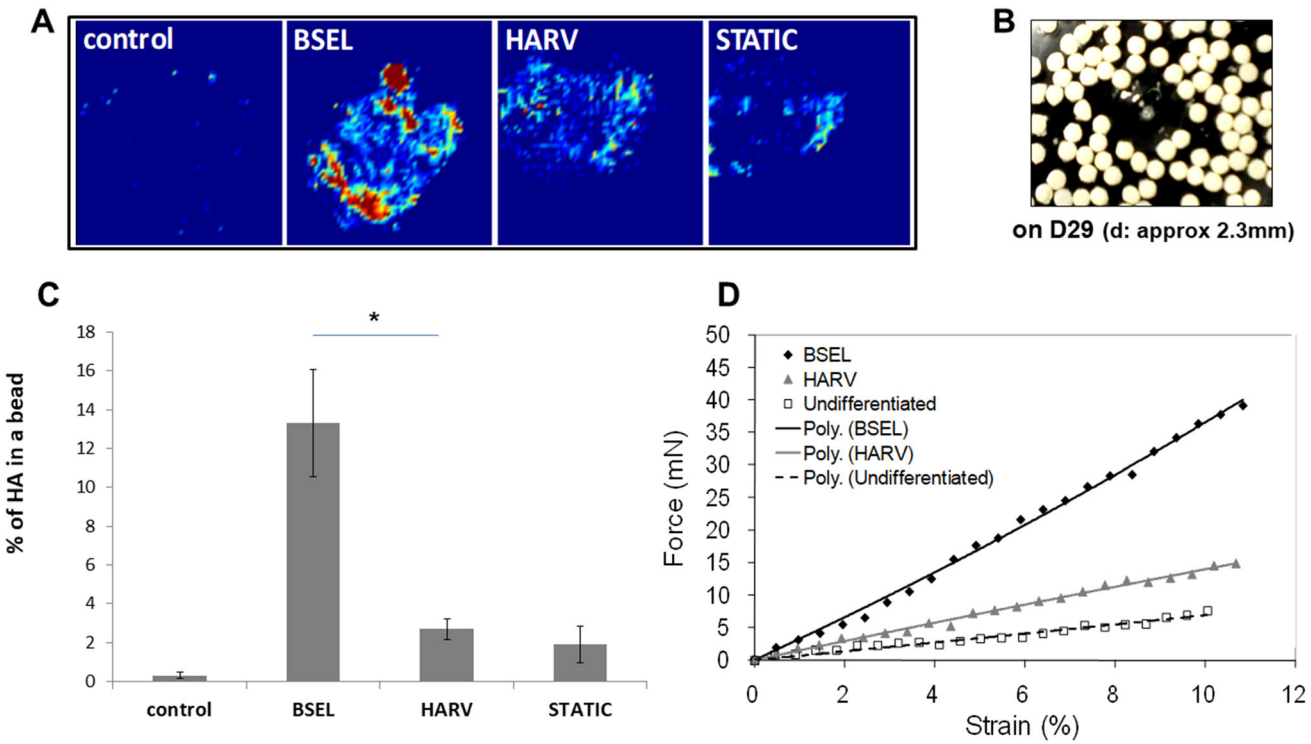

Fig. 6 Analyses of cumulated hydroxyapatite and mechanical strength of the mineralized tissue constructs collected on day 29 from all 3D-culture conditions. **A** Hydroxyapatite distribution throughout the mineralized tissue constructs was visualized by the ATR-FTIR imaging method. The infrared images were captured based on the spectral region of 1200–965 cm^{-1}. The color gradient from yellow to red represents approaching to the peak in the spectra (PO_4 at between 1026 and 1035 cm^{-1}). **B** A photo of the mineralized tissue constructs (osteogenic beads) collected on day 29 from the BSEL bioreactor. **C** Quantitative comparison of hydroxyapatite composition in the mineralized tissue constructs. The relative amount of hydroxyapatite in each of the osteogenic beads was compared by calculating the percentage area that was registered as the presence of hydroxyapatite. Statistical analysis was performed by one-way ANOVA (n = 5) at a level of significance of $p < 0.05$. All errors bars represent standard deviation (SD). **D** Mechanical strength of the mineralized tissue constructs were examined by a micro-compression testing. The force–displacement characteristics were plotted and fitted by linear regression. Corresponding Young's moduli were calculated based on this plot (Table 3)

Table 2 Medical standard of therapeutic ultrasound

Properties	Values
Frequency	1.5 MHz
PRF	1 kHz
Duty ratio	20%
Intensity	10–30 mW/cm^2

Pulse repetition frequency (PRF)

osteocalcin demonstrated more extensive expression in the defects with mineralized beads compared to the negative control group (Supplementary Fig. S3C(II) and D(II)). The strong expression of osteocalcin was found near the scattered osteocytes in the new bone tissues. We did not observe an immunogenic response or severe inflammatory cell infiltration in the cranium defects or graft resorption that typically occurs during xenogenic transplantation. In addition, there was an absence in gene expression of pluripotency markers in the mineralized tissue constructs (Fig. 5D) and there were neither tumorigenic tissues nor cartilage hypertrophy in the cranial defect sites.

3.6 Enhanced osteogenesis and mineralization via additional LIPUS stimulation

To further enhance the osteogenesis as well as mineralization of tissue constructs, we mounted the LIPUS modules on our BSEL bioreactor system (Supplementary Fig. S2). The LIPUS modules were custom-designed and supplied by Sigmax. Four ultrasound probes were evenly placed at the front of the culture chamber to ensure uniform transmission of the LIPUS (Supplementary Fig. S2A-C). LIPUS parameters, based on established medical criteria, were adjusted by a customized controller that enabled LIPUS stimulation to be applied throughout the study (Supplementary Fig. S2D and Table 2) [38]. It was verified that LIPUS was homogeneously and evenly transmitted throughout the chamber (Supplementary Fig. S2E and F). Ultrasound generates a frequency resonance that can

Table 3 Young's moduli of the Alginate bead, Control, BSEL, HARV, and STATIC groups

Groups	Young's modulus (kPa)
Alginate bead	35.23
Control	13.32
BSEL	572.1
HARV	219.2
STATIC	93.05

A control group is the hydrogels encapsulating undifferentiated ESCs with the same cell density

mechanically stimulate cells. The LIPUS stimulation customized for our BSEL bioreactor showed negligible detrimental effects on cellular viability irrespective of intensity, 10 mW/cm^2 (shown as 10 mW) or 30 mW/cm^2 (shown as 30 mW) as assessed on day 24 of culture (Fig. 7A–C). Interestingly, the gene expressions of type I collagen (Col1, Fig. 7D), osteocalcin (OC, Fig. 7E), and osteonectin (ON, Fig. 7F) demonstrated significantly augmented osteogenesis in the groups of the LIPUS stimulation (both 10 mW and 30 mW). Degree of mineralization was further enhanced by the LIPUS stimulation compared to that of the BSEL group (Fig. 7G). The FTIR analysis of the produced mineralized constructs displayed specific spectral bands that were comparable to human bone tissue (Fig. 7H) [47]. However, no statistical differences in the mechanical strength of mineralized constructs between the BSEL group and LIPUS stimulation groups were shown despite a slight increase in Young's modulus of the LIPUS constructs (Fig. 7I, Table 4).

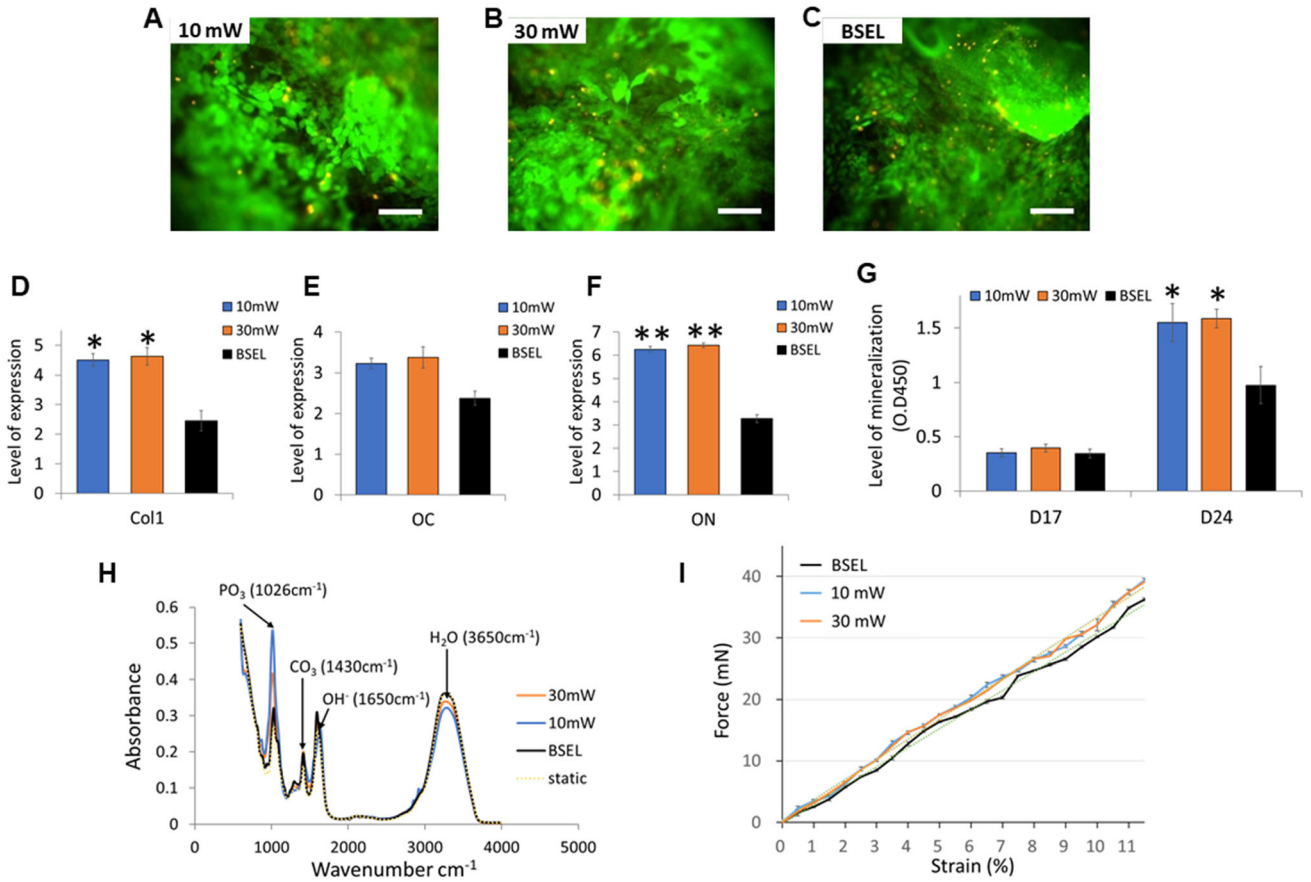

Fig. 7 Results of the mineralized tissue constructs produced by using the low-intensity pulsed ultrasound (LIPUS)-mounted BSEL bioreactor (10 mW and 30 mW). **A–C** Cell viability in the tissue constructs was examined on day 24 using a Live/Dead assay kit (live, green fluorescence; dead, red fluorescence). Scale bars indicate 200 μm. **D–F** Comparisons of osteogenic gene expressions: type I collagen (Col1; **D**), **E** Osteocalcin (OC; **E**), and Osteonectin (ON; **F**). All quantitative comparisons were normalized by the correspondent gene expression level of the Static group based on the $2^{-\Delta\Delta CT}$ method. All the statistics were done by one-way ANOVA (n = 3). All error bars represent standard deviation (SD). Asterisks indicate $p < 0.05$. **G** Comparison of mineralization based on a quantitative ARS assay. Statistical analysis was performed by one-way ANOVA (n = 5) at a level of significance of $p < 0.05$. All error bars represent standard deviation (SD). **H** FTIR spectra indicating the molecular composition of hydroxyapatite of mineralized tissue constructs. **I** Mechanical strength analysis of the mineralized tissue constructs. The force–displacement characteristics were plotted and fitted by linear regression (dotted lines). Corresponding Young's moduli were calculated based on this plot (Table 4)

Table 4 Young's moduli of the alginate bead, BSEL, 10 mW, and 30 mW groups

Groups	Young's modulus (kPa)
Alginate bead	40.53
BSEL	558.1
10 mW	594.6
30 mW	589.9

4 Discussion

In this study, we demonstrated the development of a novel automated perfusion bioreactor that was equipped with a LIPUS stimulator to produce implantable mineralized tissue constructs in a large scale. The perfusion-based BSEL bioreactor system could (1) enable the control of medium supplementation in real-time, (2) prevent metabolic waste accumulation, (3) minimize potential stresses caused by regular medium-exchange, and (4) sustain beneficial cell-secreted biomolecules during culture, thus facilitating the maintenance of a desirable environment that supports both expansion and differentiation of stem cells [48]. Our BSEL bioreactor provided a consistent maintenance of this culture environment, as well as homogenous convective mixing avoiding the generation of unnecessary turbulence. In addition, a simple but effective oxygenation was achieved by incorporating a gas-permeable membrane around the culture vessel, which enabled an immediate high gas flux with the surrounding air. This unique feature would allow different oxygen concentrations to be conveniently introduced to the stem cell culture depending on need and purpose of the experiment by simply changing a gas condition in an incubator. Moreover, the LIPUS stimulator incorporated in the BSEL bioreactor further supported 3D-osteogenesis and mineralization of stem cell-based tissue constructs.

A static culture condition that lacks a mixing would lead to insufficient mass transport into 3D tissue constructs as well as heterogeneous spatial gradients of the culture factors throughout the whole culture dish [6, 27]. In this study, low functionality of the mineralized tissues grown in the static culture was observed and verified by various examinations for osteogenic tissue formation such as osteogenic gene expression, mineralization, and hydroxyapatite accumulation. In terms of growth kinetics, the BSEL group showed the fastest growth rate, specifically during the early differentiation period from day 5 to 9. When HepG2-CM was replaced by the osteogenic medium on day 3, the BSEL bioreactor allowed cells to naturally adapt to the new culture medium by a slow rate of medium perfusion (0.7 μl/s). On the contrary, cells in the HARV group experienced an abrupt change in the culture environment while the entire culture medium was exchanged at once. Furthermore, the profiles of metabolite accumulation showed that the ammonia concentration of the HARV group was sustained at significantly higher levels during the culture period (between 2.0 and 3.5 mM), whereas that of the BSEL group was maintained at lower levels (mostly between 1 and 1.5 mM). Given an ammonia concentration higher than 2 mM was reported to be inhibitory to the cellular growth in ESC cultures [49], our BSEL bioreactor could offer a beneficial environment for the long-term culture of ESCs as maintaining the ammonia concentrations lower than 2 mM during the culture period. In addition, lower pH levels (mostly below 7.0) of the HARV group shown during the culture period could also disrupt cellular metabolism as osteogenic differentiation progressed [49]. Therefore, the faster cell growth rate of the BSEL bioreactor could be attributed to the continuous medium perfusion, which resulted in densely packed contacts between differentiating ESCs and efficient 3D-osteogenesis [50]. Meanwhile, the early embryo development of human and mouse was reported to progress in physiological glucose levels (about 5 mM) and show high dependency on pyruvate or glutamine contents instead of glucose [51, 52]. However, our results showed that differentiating ESCs survived in 0 mM of glucose, thus adapting to other substrates present in the medium such as pyruvate and glutamine [53]. The bioprofile of glutamine levels on our study implied that the ESCs were differentiated with glutamine consumption. Glucose levels in all groups reached almost 0 mM, as our osteogenic medium was based on the low glucose αMEM (5 mM) but contained high concentrations of various amino acids and vitamins, and sodium pyruvate. Medium perfusion in the BSEL bioreactor maintained significantly higher steady levels of glutamine during the culture period.

A significantly upregulated Osterix expression ($p < 0.001$) was found in the BSEL group while type I collagen and Runx2 did not show significant differences between both the bioreactor groups (HARV and BSEL). Previous studies revealed that the expression of Runx2 represents the differentiation into pre-osteoblasts that are still bi-potential, whereas Osterix regulates the later stage of osteoblast differentiation with bone matrix deposition, acting downstream of Runx2 [54–56]. The osteogenic gene expressions in this study were in agreement with the previous studies, showing better functionality of mineralized tissue constructs resulted from the BSEL group with the highest Osterix expression, which were analyzed by accumulated mineralization, hydroxyapatite composition, and mechanical strength. In addition, an appendicular critical defect model using adult New Zealand rabbits allowed us to test *in vivo* efficacy of the mineralized tissue constructs

produced by our BSEL bioreactor. The promising results from this animal study suggest that the insertion of highly integrated mineralized tissue constructs could promote the effective regeneration of a critical-sized bone defect.

The LIPUS stimulation additionally mounted on the BSEL bioreactor resulted in further higher enhancement of osteogenesis and mineralization of stem cell-based tissue constructs compared to the original BSEL bioreactor without LIPUS modules. However, such results were not followed by a significant increase in the mechanical property. To maximize bone tissue functionality including strengthened mechanical property, the LIPUS stimulation parameters should be optimized in the operation of the BSEL bioreactor. In addition, the mechano-transduction pathway involved in the cellular responses caused by the LIPUS stimulation remains unclear. We speculate that the underlying mechanism is based on increased calcium ion transportation through cell membrane in response to the LIPUS stimulation, as it plays a crucial role in osteogenic differentiation [57]. Further ongoing studies in our group would deliver valuable information needed to optimize the LIPUS stimulation procedures on our bioreactor while verifying the multiple key factors that drive the reinforced bone tissue functionality.

In conclusion, the bioreactor system newly developed in this study successfully achieved consistent maintenance of an ideal environment for a long-term 3D stem cell culture in a large scale, which was supported by the controlled medium perfusion, RWV mechanism, and effective oxygenation system. In addition, the LIPUS module incorporated in the bioreactor further supported 3D-osteogenesis and mineralization of stem cell-based tissue constructs. We believe that this study has meaningful implications to clinical practice as suggesting a "one-stage" biomanufacturing process with minimizing operator handling that leads to the feasibility of "off-the-shelf" production of functional tissue constructs.

Supplementary Information The online version contains supplementary material available at https://doi.org/10.1007/s13770-022-00447-3.

Acknowledgements This research was supported by Incheon National University (International Cooperative) Research Grant in 2019.

Author contributions Jae Min Cha, PhD and Athanasios Mantalaris, PhD: Administrative support, Conception and design, Manuscript writing, review & editing. Yu-Shik Hwang, PhD, Dong-Ku Kang, PhD, and Elana S Cooper, MSc: Manuscript writing, Data analysis and interpretation. Jun Lee, DDS, PhD: Collection and assembly of data.

Declarations

Conflict of interest No competing financial interests exist.

Ethical statement The animal studies were performed after receiving approval of the Institutional Animal Care and Use Committee (IACUC) in Wonkwang University (IACUC approval No. WKU21-37).

References

1. Polak JM, Mantalaris S. Stem cells bioprocessing: An important milestone to move regenerative medicine research into the clinical arena. Pediatr Res. 2008;63:461–6.
2. Peroglio M, Gaspar D, Zeugolis DI, Alini M. Relevance of bioreactors and whole tissue cultures for the translation of new therapies to humans. J Orthop Res. 2018;36:10–21.
3. Cha JM, Shin EK, Sung JH, Moon GJ, Kim EH, Cho YH, et al. Efficient scalable production of therapeutic microvesicles derived from human mesenchymal stem cells. Sci Rep. 2018;8:1171.
4. Gieseck RL 3rd, Hannan NR, Bort R, Hanley NA, Drake RA, Cameron GW, et al. Maturation of induced pluripotent stem cell derived hepatocytes by 3D-culture. PloS One. 2014;9:e86372.
5. Xie Y, Hardouin P, Zhu Z, Tang T, Dai K, Lu J. Three-dimensional flow perfusion culture system for stem cell proliferation inside the critical-size beta-tricalcium phosphate scaffold. Tissue Eng. 2006;12:3535–43.
6. Zhao F, Pathi P, Grayson W, Xing Q, Locke BR, Ma T. Effects of oxygen transport on 3-d human mesenchymal stem cell metabolic activity in perfusion and static cultures: experiments and mathematical model. Biotechnol Prog. 2005;21:1269–80.
7. Cha JM, Mantalaris A, Jung S, Ji Y, Bang OY, Bae H. Mesoderm lineage 3D tissue constructs are produced at large-scale in a 3D stem cell bioprocess. Biotechnol J. 2017;12:1600748.
8. Ishaug SL, Crane GM, Miller MJ, Yasko AW, Yaszemski MJ, Mikos AG. Bone formation by three-dimensional stromal osteoblast culture in biodegradable polymer scaffolds. J Biomed Mater Res. 1997;36:17–28.
9. Martin I, Obradovic B, Freed LE, Vunjak-Novakovic G. Method for quantitative analysis of glycosaminoglycan distribution in cultured natural and engineered cartilage. Ann Biomed Eng. 1999;27:656–62.
10. Cameron CM, Hu WS, Kaufman DS. Improved development of human embryonic stem cell-derived embryoid bodies by stirred vessel cultivation. Biotechnol Bioeng. 2006;94:938–48.
11. Fok EY, Zandstra PW. Shear-controlled single-step mouse embryonic stem cell expansion and embryoid body-based differentiation. Stem Cells. 2005;23:1333–42.
12. Kehoe DE, Lock LT, Parikh A, Tzanakakis ES. Propagation of embryonic stem cells in stirred suspension without serum. Biotechnol Prog. 2008;24:1342–52.
13. Niebruegge S, Bauwens CL, Peerani R, Thavandiran N, Masse S, Sevaptisidis E, et al. Generation of human embryonic stem cell-derived mesoderm and cardiac cells using size-specified aggregates in an oxygen-controlled bioreactor. Biotechnol Bioeng. 2009;102:493–507.
14. Niebruegge S, Nehring A, Bär H, Schroeder M, Zweigerdt R, Lehmann J. Cardiomyocyte production in mass suspension culture: embryonic stem cells as a source for great amounts of functional cardiomyocytes. Tissue Eng Part A. 2008;14:1591–601.
15. Schroeder M, Niebruegge S, Werner A, Willbold E, Burg M, Ruediger M, et al. Differentiation and lineage selection of mouse embryonic stem cells in a stirred bench scale bioreactor with automated process control. Biotechnol Bioeng. 2005;92:920–33.
16. Abranches E, Bekman E, Henrique D, Cabral JM. Expansion of mouse embryonic stem cells on microcarriers. Biotechnol Bioeng. 2007;96:1211–21.

17. Dang SM, Gerecht-Nir S, Chen J, Itskovitz-Eldor J, Zandstra PW. Controlled, scalable embryonic stem cell differentiation culture. Stem Cells. 2004;22:275–82.
18. Wang X, Wei G, Yu W, Zhao Y, Yu X, Ma X. Scalable producing embryoid bodies by rotary cell culture system and constructing engineered cardiac tissue with ES-derived cardiomyocytes in vitro. Biotechnol Prog. 2006;22:811–8.
19. Placzek MR, Chung IM, Macedo HM, Ismail S, Mortera Blanco T, Lim M, et al. Stem cell bioprocessing: fundamentals and principles. J R Soc Interface. 2009;6:209–32.
20. Dang SM, Kyba M, Perlingeiro R, Daley GQ, Zandstra PW. Efficiency of embryoid body formation and hematopoietic development from embryonic stem cells in different culture systems. Biotechnol Bioeng. 2002;78:442–53.
21. Freed LE, Vunjaknovakovic G. Cultivation of cell-polymer tissue constructs in simulated microgravity. Biotechnol Bioeng. 1995;46:306–13.
22. Gerecht-Nir S, Cohen S, Itskovitz-Eldor J. Bioreactor cultivation enhances the efficiency of human embryoid body (hEB) formation and differentiation. Biotechnol Bioeng. 2004;86:493–502.
23. Hwang YS, Cho J, Tay F, Heng JY, Ho R, Kazarian SG, et al. The use of murine embryonic stem cells, alginate encapsulation, and rotary microgravity bioreactor in bone tissue engineering. Biomaterials. 2009;30:499–507.
24. Lü S, Liu S, He W, Duan C, Li Y, Liu Z, et al. Bioreactor cultivation enhances NTEB formation and differentiation of NTES cells into cardiomyocytes. Cloning Stem Cells. 2008;10:363–70.
25. Randle WL, Cha JM, Hwang YS, Chan KL, Kazarian SG, Polak JM, et al. Integrated 3-dimensional expansion and osteogenic differentiation of murine embryonic stem cells. Tissue Eng. 2007;13:2957–70.
26. Siti-Ismail N, Bishop AE, Polak JM, Mantalaris A. The benefit of human embryonic stem cell encapsulation for prolonged feeder-free maintenance. Biomaterials. 2008;29:3946–52.
27. Liu M, Liu N, Zang R, Li Y, Yang ST. Engineering stem cell niches in bioreactors. World J Stem Cells. 2013;5:124–35.
28. Cha JM, Lee MY, Hong J. Bioreactor systems are essentially required for stem cell bioprocessing. Precis Future Med. 2019;3:19–23.
29. de Peppo GM, Marcos-Campos I, Kahler DJ, Alsalman D, Shang L, Vunjak-Novakovic G, et al. Engineering bone tissue substitutes from human induced pluripotent stem cells. Proc Natl Acad Sci U S A. 2013;110:8680–5.
30. Marolt D, Campos IM, Bhumiratana S, Koren A, Petridis P, Zhang G, et al. Engineering bone tissue from human embryonic stem cells. Proc Natl Acad Sci U S A. 2012;109:8705–9.
31. Panciera T, Azzolin L, Cordenonsi M, Piccolo S. Mechanobiology of YAP and TAZ in physiology and disease. Nat Rev Mol Cell Biol. 2017;18:758–70.
32. Yavropoulou MP, Yovos JG. The molecular basis of bone mechanotransduction. J Musculoskelet Neuronal Interact. 2016;16:221–36.
33. Perry MJ, Parry LK, Burton VJ, Gheduzzi S, Beresford JN, Humphrey VF, et al. Ultrasound mimics the effect of mechanical loading on bone formation in vivo on rat ulnae. Med Eng Phys. 2009;31:42–7.
34. Padilla F, Puts R, Vico L, Raum K. Stimulation of bone repair with ultrasound: a review of the possible mechanic effects. Ultrasonics. 2014;54:1125–45.
35. Rutten S, Nolte PA, Guit GL, Bouman DE, Albers GH. Use of low-intensity pulsed ultrasound for posttraumatic nonunions of the tibia: a review of patients treated in the Netherlands. J Trauma. 2007;62:902–8.
36. Gilbert SJ, Stevens J, Vishwakarma AR, Archer CW, Duance VC. The use of pulsed low-intensity ultrasound (PLIUS) as a therapy for cartilage repair. Int J Exp Pathol. 2014;95:A12.
37. Calik M, Calik SG, Yilmaz H, Karaca G, Esen H, Avunduk MC, et al. Using low-intensity pulsed ultrasound to stimulate the consolidation of rib fractures: an experimental study. Eur Clin Respir J. 2014;44:1924.
38. Harrison A, Lin S, Pounder N, Mikuni-Takagaki Y. Mode & mechanism of low intensity pulsed ultrasound (LIPUS) in fracture repair. Ultrasonics. 2016;70:45–52.
39. Hwang YS, Randle WL, Bielby RC, Polak JM, Mantalaris A. Enhanced derivation of osteogenic cells from murine embryonic stem cells after treatment with HepG2-conditioned medium and modulation of the embryoid body formation period: application to skeletal tissue engineering. Tissue Eng. 2006;12:1381–92.
40. Rathjen J, Lake JA, Bettess MD, Washington JM, Chapman G, Rathjen PD. Formation of a primitive ectoderm like cell population, EPL cells, from ES cells in response to biologically derived factors. J Cell Sci. 1999;112:601–12.
41. Livak KJ, Schmittgen TD. Analysis of relative gene expression data using real-time quantitative PCR and the 2(-Delta Delta C(T)) Method. Methods. 2001;25:402–8.
42. Gregory CA, Gunn WG, Peister A, Prockop DJ. An Alizarin red-based assay of mineralization by adherent cells in culture: comparison with cetylpyridinium chloride extraction. Anal Biochem. 2004;329:77–84.
43. Kazarian SG, Chan KLA. "Chemical photography" of drug release. Macromolecules. 2003;36:9866–72.
44. Zhang GJ, Moore DJ, Flach CR, Mendelsohn R. Vibrational microscopy and imaging of skin: from single cells to intact tissue. Anal Bioanal Chem. 2007;387:1591–9.
45. Andrei DC, Briscoe BJ, Luckham PF, Williams DR. The deformation of microscopic gel particles. J Chim Phys Physicochim Biol. 1996;93:960–76.
46. Briscoe BJ, Liu KK, Williams DR. Adhesive contact deformation of a single microelastomeric sphere. J Colloid Interface Sci. 1998;200:256–64.
47. Karp JM, Ferreira LS, Khademhosseini A, Kwon AH, Yeh J, Langer RS. Cultivation of human embryonic stem cells without the embryoid body step enhances osteogenesis in vitro. Stem Cells. 2006;24:835–43.
48. Bauwens C, Yin T, Dang S, Peerani R, Zandstra PW. Development of a perfusion fed bioreactor for embryonic stem cell-derived cardiomyocyte generation: oxygen-mediated enhancement of cardiomyocyte output. Biotechnol Bioeng. 2005;90:452–61.
49. Cormier JT, Zur Nieden NI, Rancourt DE, Kallos MS. Expansion of undifferentiated murine embryonic stem cells as aggregates in suspension culture bioreactors. Tissue Eng. 2006;12:3233–45.
50. Smith AG. Mouse embryo stem cells: their identification, propagation and manipulation. Semin Cell Biol. 1992;3:385–99.
51. Conaghan J, Handyside AH, Winston RM, Leese HJ. Effects of pyruvate and glucose on the development of human preimplantation embryos in vitro. Reprod Fertil. 1993;99:87–95.
52. Quinn P. Enhanced results in mouse and human embryo culture using a modified human tubal fluid medium lacking glucose and phosphate. J Assist Reprod Genet. 1995;12:97–105.
53. Khoo ML, McQuade LR, Smith MSR, Lees JG, Sidhu KS, Tuch BE. Growth and differentiation of embryoid bodies derived from human embryonic stem cells: effect of glucose and basic fibroblast growth factor. Biol Reprod. 2005;73:1147–56.
54. Nakashima K, Zhou X, Kunkel G, Zhang Z, Deng JM, Behringer RR, et al. The novel zinc finger-containing transcription factor osterix is required for osteoblast differentiation and bone formation. Cell. 2002;108:17–29.

55. Ducy P, Zhang R, Geoffroy V, Ridall AL, Karsenty G. Osf2/Cbfa1: a transcriptional activator of osteoblast differentiation. Cell. 1997;89:747–54.
56. Komori T, Yagi H, Nomura S, Yamaguchi A, Sasaki K, Deguchi K, et al. Targeted disruption of Cbfa1 results in a complete lack of bone formation owing to maturational arrest of osteoblasts. Cell. 1997;89:755–64.
57. Zhang S, Cheng J, Qin YX. Mechanobiological modulation of cytoskeleton and calcium influx in osteoblastic cells by short-term focused acoustic radiation force. PLoS One. 2012;7:e38343.